Available online at www.sciencedirect.com
SCIENCE DIRECT®
Acta Materialia 52 (2004) 3383–3402
Acta MATERIALIA
www.actamat-journals.com

Stress dependence of the hysteresis in single crystal NiTi alloys

R.F. Hamilton [a], H. Sehitoglu [a,*], Y. Chumlyakov [b], H.J. Maier [c]

[a] Department of Mechanical and Industrial Engineering, University of Illinois at Urbana-Champaign, 140 Mechanical Engineering Building, MC-244, 1206 West Green Street, Urbana, IL 61801, USA
[b] Siberian Physical Technical Institute, 1, Novo-Sobornay, 634050 Tomsk, Russia
[c] University Paderborn, Lehrstuhl für Werkstoffkunde, 33098 Paderborn, Germany

Received 26 November 2003; received in revised form 22 March 2004; accepted 22 March 2004
Available online 6 May 2004

Abstract

We demonstrate the variation in thermal hysteresis with increasing external stress for reversible martensitic transformations. The hysteresis was measured in temperature cycling experiments under external stress and also under pseudoleastic deformation conditions. To understand the role of composition and crystal orientation effects, the study included aged and solutionized Ti–50.1, Ti–50.4, Ti–50.8 and Ti–51.5at.%Ni in the [1 1 1], [0 0 1], [0 1 1], [0 1 2], and [1 2 3] orientations. Differential scanning calorimetry was used to characterize the thermal hysteresis resulting from thermal cycling under zero stress. The results show unequivocally that the thermal hysteresis expands with increasing external stress for aged and solutionized Ti–50.1at.%Ni and Ti–50.4at.%Ni alloys, while it contracts with increasing external stress for the higher Ni alloys with 50.8 and 51.5at.%Ni compositions. The growth of temperature hysteresis was from 20 °C to as high as 80 °C for the lower Ni alloys, while the contraction of the hysteresis was from 60 to 15 °C for the higher Ni alloys. The stress dependence of the hysteresis is rationalized considering dissipation of elastic strain energy due to relaxation of coherency strains at martensite–austenite interfaces. The role of precipitates and frictional work on transformation hysteresis is also clarified based on experiments on low and high Ni alloys with heterogeneous and homogenous precipitate structures respectively. A micro-mechanical model based on reversible thermodynamics was modified to account for plastic relaxation of coherent transforming interfaces, and the predictions account for the growing hysteresis with increasing external stress.

Keywords: Hysteresis; Shape memory; Elastic strain energy; Phase transformation

1. Introduction

1.1. Background on hysteresis in shape memory alloys

In this paper, we address the nature of the hysteresis in shape memory alloys, which plays a considerable role in design and utilization of these materials. To begin with, basic concepts pertinent to thermodynamics of martensitic transformations are introduced. These provide background for a subsequent review of fundamental aspects of the hysteresis in shape memory alloys. Martensitic transformations are considered thermoelastic if the martensite reverts to the parent phase in its original orientation upon heating. Consequently, the strains associated with the forward transformation (austenite to martensite) are totally recovered during the reverse transformation (martensite to austenite). Thermoelastic equilibrium at a transforming interface requires a local balance between chemical and non-chemical contributions to the total Gibbs free energy of the system. The chemical constituent is a result of the chemical energy difference between the austenitic and martensitic phases due to the nature of bonding in the crystalline phases. The non-chemical constituent is separated into reversible and irreversible components.

Elastic strain energy provides the reversible non-chemical contribution to the overall free energy of the system. The method of elastic strain energy generation depends upon whether or not external stress is applied. In the absence of external stress, the martensite trans-

* Corresponding author. Tel.: +1-217-333-4112; fax: +1-217-244-6534.
E-mail address: huseyin@uiuc.edu (H. Sehitoglu).

1359-6454/$30.00 © 2004 Acta Materialia Inc. Published by Elsevier Ltd. All rights reserved.
doi:10.1016/j.actamat.2004.03.038

Nomenclature

$\sum_{ij}$	macroscopic average external stress	ε_{ij}^{tr}	local transformation strain in a single crystal
E_{ij}	average strain field in a single crystal	ε_{ij}^{n}	intrinsic transformation strain for the nth variant
E_{ij}^{e}	average elastic strain field in a single crystal	σ_{ij}	local stress due to the existing martensite variants
B	material constant	σ_{ij}^{dist}	local disturbance stress in a martensite variant
T_0	phase equilibrium temperature	f^n	volume fraction of martensite for the nth variant
I_{klrs}	identity tensor	H_M	temperature hysteresis
C_{ijkl}	elasticity tensor		
S_{ijkl}	Eshelby tensor		
ε_{ij}^{e}	local elastic strain in a single crystal		

formations in NiTi produce a self-accommodating arrangement of martensite correspondent variant pairs (CVPs) that minimizes elastic strain energy. As the volume fraction of self-accommodating groups (SAGs) of martensite CVPs grows, the concomitant increases in interfacial energy and elastic strain raise the stored elastic strain energy of the system. In the presence of external stress, martensite CVPs that are oriented favorably to the external stress grow, at the expense of unfavorable CVPs within SAGs, accumulating stored elastic strain energy due to the escalating transformation strain. Similar to an external stress, a precipitate stress field induces preferentially oriented martensite variants. Therefore, the elastic strain energy evolution for an aged material proceeds to form a martensite microstructure consisting of precipitate stress-induced martensite variants in addition to SAGs and external stress-induced martensite.

The irreversible component of the non-chemical energy is mainly related to two energy dissipative processes. One process is attributed to energy dissipated in the form of frictional work [1–5]. Frictional work is spent overcoming resistance to interfacial motion, the resistance scales with the strength of the parent phase. The second dissipative process is due to the dissipation of elastic strain energy. Stored elastic strain energy is dissipated when the coherency strains of martensite–austenite interfaces relax [1–11]. Therefore, plastic accommodation causes dissipation of elastic strain energy. Relaxation of coherency strains as an interface advances will also occur when it bypasses dislocations or precipitates [4,6,10,11].

We now outline the effects precipitates have on the martensite morphology, stored elastic strain energy, and elastic strain energy dissipation. Changes in the stored elastic energy depend on precipitate coherency [4,6,10]. Hornbogen [6] proposes that initially coherent precipitates shear during the transformation thus remaining coherent with the martensite phase. In this case, as the transformation front advances, the stored elastic energy increases. However, depending on the slip resistance of the matrix, the precipitate size and transformation strains, the precipitates could become incoherent after the transformation. In this case, the dislocations inherited by the martensite from the incoherent precipitate boundaries produce relaxation of martensite–austenite interface coherency strains causing stored elastic strain energy dissipation. Delaey et al. [4] have reached similar conclusions that not all the energy required to shear the particle initially is necessary to keep the particle sheared coherently with the martensite matrix, thus part of the stored elastic strain energy is relaxed.

The ramifications of the aforementioned different energy contributions on the shape memory behavior are best-conveyed using Figs. 1 and 2. The role of elastic strain energy in the absence of energy dissipation is presented in Fig. 1(a) and (b), and the role of frictional and elastic strain energy dissipation is outlined in Fig. 1(c) and (d). Fig. 1(a) illustrates a thermoelastic martensitic transformation in which the non-chemical free energy consists only of reversible elastic strain energy. In this case, elastic strain energy stored during the forward transformation is reversibly recovered during the reverse transformation [1] so the forward and reverse transformations follow the same thermal path without a hysteresis. Elastic strain energy provides opposition to the forward transformation, thus further transformation requires additional under-cooling (cooling below T_0). Therefore, the austenite to martensite transformation is completed at T_f. On the other hand, elastic strain energy stored during the forward transformation assists the reverse transformation. In the absence of energy dissipative mechanisms, stored elastic energy allows completion of the reverse transformation prior to T_0 as illustrated in Fig. 1(a). In Fig. 1(b), the martensitic transformation is ideally reversible because non-chemical contributions are not considered; therefore, the forward and reverse transformations occur at the phase equilibrium temperature, T_0. Note that the under-cooling, facilitated by accruing elastic strain energy, inclines the curve in Fig. 1(a) compared to Fig. 1(b).

Fig. 1(c) and (d) present dissipative mechanisms that give rise to the hysteresis. Fig. 1(c) illustrates how frictional work dissipated due to resistance to interfacial motion compels additional undercooling and overheating causing the start temperatures for the forward and

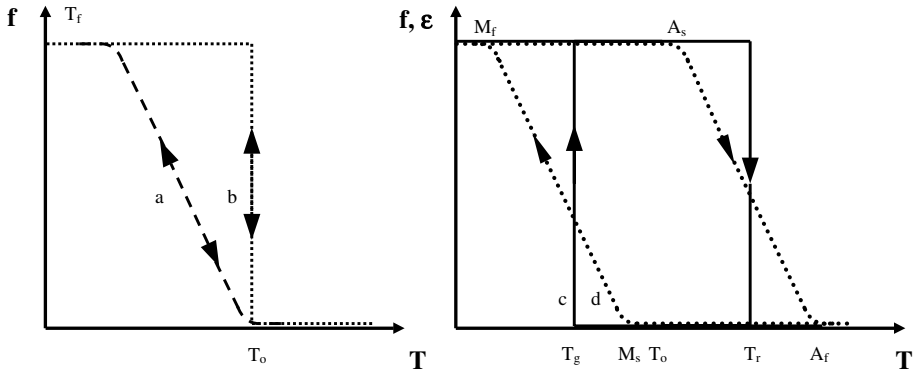

Fig. 1. (a) Single transformation path (martensite volume fraction (f vs. temperature T) for forward and reverse transformations due to chemical contribution and reversible elastic strain energy. The forward transformation starts at T_0 and ends at T_f, and the reverse transformation starts at T_f and ends at T_0. The slope of the curve is attributed to stored elastic strain energy. (b) Transformation path in the absence of non-chemical contributions to the total Gibbs free energy. The forward and reverse transformations take place at the phase equilibrium temperature T_0. (c) Idealized f–T hysteresis attributed to frictional resistance only. The forward transformation occurs at T_g, and the reverse transformation occurs at T_r. (d) Idealized schematic of a strain (ε)–temperature (T) hysteresis illustrating the combined effect of stored elastic strain energy, frictional resistance to interfacial motion, and stored elastic strain energy dissipation. Forward and reverse transformations now start and end at M_s, A_s and M_f, A_f, respectively.

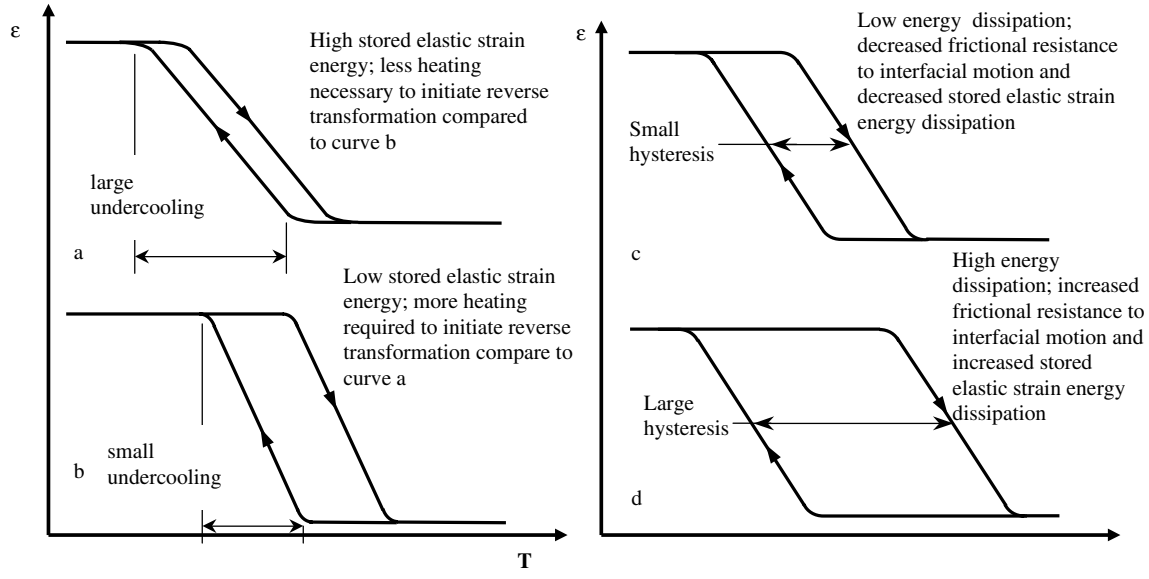

Fig. 2. Idealized schematics of strain–temperature curves. (a and b) The effect of elastic strain energy on the hysteresis cycle. (c and d) The effect of energy dissipation on the hysteresis cycle.

reverse transformations to decrease and increase respectively. In the figure, stored elastic strain energy is ignored and the frictional resistance is constant during the reverse and forward transformations. With these assumptions, the forward and reverse transformations start and finish at the constant temperatures T_g and T_r respectively. This would be the case for a single-crystal, single interface transformation in which no elastic strain energy is stored because the transformational shape change takes place against the atmosphere as the interface traverses the specimen [3]. Fig. 1(d) is an idealized schematic of a strain–temperature curve that is representative of the hysteresis profiles considered in this study. Evolution of stored elastic strain energy and variable frictional dissipation give rise to the slope of the curve. As a result of stored elastic strain energy dissipation, less elastic strain energy is available to assist the reverse transformation. Therefore, increased chemical energy is required (i.e. A_s increases) to initiate and complete the reverse transformation, which widens the hysteresis. As discussed earlier, frictional resistance to interfacial motion influences the hysteresis size in Fig. 1(d) as well. The reverse transformation temperatures, A_s and A_f, and thus the hysteresis would be lower when both dissipative mechanisms are minimized.

We now consider Fig. 2, which exposes the impact of various degrees of stored elastic strain energy and energy dissipation on the strain-temperature hysteresis.

Fig. 2(a) and (b) elucidate how stored elastic strain energy evolution determines under-cooling hence changing the slope of the hysteresis curve. When stored elastic strain energy is high (Fig. 2(a)), the slope of the curve is shallow, whereas when stored elastic strain energy is low (Fig. 2(b)), the slope of the curve is steep. Fig. 2(a) represents the response when precipitates undergo coherent shearing as the martensite front passes them. Fig. 2(b) illustrates the results when precipitate coherency strains are lower. Fig. 2(c) and (d) highlight the role of various degrees of energy dissipation on hysteresis width. The narrow hysteresis in Fig. 2(c) corresponds to minimal energy dissipation ascribed to frictional work and elastic strain energy relaxation. This occurs when the martensite motion occurs without hindrance from the incoherent precipitate structure. On the contrary, initially coherent precipitates that lose coherency leads to the wider hysteresis as shown in Fig. 2(d).

1.2. Motivation of the current study

In previous work, the origins of potential dissipative mechanisms have not been clarified, and the factors that influence these mechanisms (i.e. external stress fields, matrix strength properties, precipitate microstructure, plastic accommodation, detwinning, etc.) have not been investigated with rigorous experimentation. In the current work, we used an extensive experimental investigation of the hysteresis in single crystal NiTi alloys to study the factors that influence the dissipative mechanisms. Transmission electron microscopy (TEM) provides microstructure evidence to help rationalize the hysteresis behavior by revealing the initial precipitate microstructure as well as the dislocation arrangements resulting from repeated thermal cycling. To eliminate the influence of grain boundaries and prior cold-work, cast single crystals were investigated.

To scrutinize the role of strength properties of the matrix, different compositions of NiTi, Ti–50.1at.%Ni, Ti–50.4at.%Ni, Ti–50.8at.%Ni, and Ti–51.5at.%Ni, were investigated. To study the influence of age hardening, both aged (823 K, 1.5 h) and solutionized alloys are considered. Since the precipitate volume fraction will be different for each alloy, the inter-particle distance and precipitate/matrix interface will differ for each alloy. Accordingly, aging provides a means to assess how the precipitate microstructure influences elastic strain energy. Since matrix strength alters frictional resistance to interfacial motion, the choice of compositions and age hardening provides insight into this energy dissipative mechanism. The different crystal orientations chosen correspond to different resolved shear stress factors (RSSF) for slip in the austenite ([0 0 1] vs. [1 2 3] (or [1 1 1]) [12]. Also, the elastic strain energy increases as the volume fraction of martensite favorably oriented to the external stress increases, reorients, and detwins. Maximum transformation strains differ significantly for the hard [0 0 1] orientation compared to the softer [1 1 1] and [1 2 3] orientations [12,13]. Multiple CVPs are activated for the [0 0 1] and [1 1 1] orientations, but only one is activated for the [1 2 3] orientation [13]. Multiple martensite variant interface interactions may relax stored elastic energy. Therefore, the choice of orientations provides useful insight. To predict the growing hysteresis due to elastic strain energy dissipation, we modify an earlier thermodynamics formulation [14–16] and provide intuitive predictions of the observed behavior particularly for lower Ni alloys.

2. Experimental techniques

Special Metals Corporation, New York, supplied the cast ingots that were produced via vacuum induction melting followed by vacuum arc remelting. These cast ingots were then grown into single crystals of random orientation in an inert gas atmosphere using the Bridgman technique. Single crystal ingots were solutionized at 920 °C for 24 h in a vacuum furnace and then quenched. Laue back-scatter diffraction patterns indicated the orientation of the single crystal bulk ingot. Circular disks were cut from the ingots at an angle that would provide specimens of the desired orientation. Dog-bone type, small scale test specimens were electro-discharge machined from the disks to have a 8 mm (height) × 3 mm (width) × 1.5 mm (thickness) gauge section. Solutionizing of the dog-bone specimens was conducted at 1273 K for 2 h in an inert gas atmosphere and the specimens were subsequently quenched. Aging at 823 K for 1.5 h was carried out in a Lindberg/Blue 1200 °C box furnace BF51732 series followed by water quenching.

A uniaxial tensile stress was applied to the specimen and held constant during the temperature cycling. Temperature cycling started with cooling from room temperature to −100 °C, followed by heating to 90 °C, and finally the specimen was cooled to room temperature. Heating and cooling rates were approximately 10 °C per minute to promote uniform temperature changes throughout the specimen. Heating was accomplished using induction heating of the specimen grips, and liquid nitrogen flowed through copper tubing to cool the grips, which cooled the specimen through conduction. The external stress was increased incrementally until either the transformation strain saturated or the specimen showed a significant level of unrecoverable (plastic) strain. A miniature extensometer recorded strain measurements in the gauge section while the specimen temperature was recorded using a thermocouple affixed to the gauge section.

Small, approximately 20 mg, samples were cut from solutionized tension specimens for differential scanning calorimetry (DSC) analysis. Following etching, some

DSC specimens were aged at 823 K for 1.5 h. A Perkin–Elmer Instruments Pyris 1 power-compensated DSC provided heat flow vs. temperature data under zero stress. Heating and cooling rates were 10 °C per minute. First, the specimens were heated to 100 °C and held at the temperature for 3 min to ensure that the microstructure is fully austenitic. Next, the specimens were cooled to −100 °C and held there for 3 min to obtain a fully martensitic microstructure. The specimens were then heated to 100 °C followed by cooling to room temperature.

3. Thermomechanical modeling

Micro-mechanics and thermodynamics have been combined to model strain-temperature behavior. The models by Patoor et al. [14,15], Gall et al. [16], Gabry et al. [17], Sun and Hwang [18], and Huang and Brinson [19] do not capture hysteresis growth/shrinkage with increasing external stress observed in thermal cycling experiments under constant-load. Each of the formulations includes an interaction energy term that represents the resistive contribution accounting for increasing volume fraction of martensite as well as interacting groups of self-accommodating variants. The model proposed by Gabry et al. [17] has the capability to predict hysteresis changes. They consider a three phase system made up of austenite, self-accommodating martensite, and oriented martensite instead of incorporating interaction energy. Two models consider the effect of plasticity, characterized by unrecoverable strain, on the analysis of shape memory behavior. Zhang and McCormick [20] subtract the plastic strain from the crystallographic transformation strain but the interaction energy contribution remains unaffected. Bo and Lagoudas [21] account for plastic strain using a back stress term as the average of the local stresses resulting from microstructure changes caused by phase transformation and plastic deformations. For their model, interaction energy is considered using a drag stress term to account for the contributions of elastic interactions due to the creation of martensite variants. Although these models consider plasticity, the hysteresis is constant with increasing stress. To satisfy the second law of thermodynamics, each of the models [14–21] incorporated a dissipative potential for the forward and reverse transformations.

In the current study, the model of Patoor et al. [14] and Gall et al. [16] is adapted to account for stored elastic strain energy dissipation due to plastic relaxation of coherent stresses at martensite–austenite interfaces in the interaction energy. Although, we believe that age hardening and matrix strength affect the hysteresis size, TEM reveals outstanding contrasts in the dislocation densities of low vs. high Ni alloys. It should be noted that we distinguish between plastic deformation that results in strain energy relaxation at the transforming phase boundary and plastic deformation that leads to unrecoverable (remnant) strain. We attribute relaxation of elastic strain energy storage to dislocation emissions at the austenite/martensite phase boundary that lower coherent interface strains. The effect of relaxation of coherent interface strains can be seen without significant levels of remnant strain. Figs. 6 and 10 show no remnant strain, but the hysteresis increases and decreases respectively for the two cases. Therefore, our proposed ideas provide a strong background for future consideration of the details of plasticity effects on hysteresis behavior.

Plastic relaxation causes a reduction in transformation strain energy. This is analogous to the well-known dislocation generation mechanism studied by Johnson et al. and Ashby et al. [22,23] for growing, coherent precipitate interfaces. In our case, the dislocation loops at the martensite/austenite interfaces grow as the transformation front advances. A thermo-micromechanics framework was developed, and the thermodynamic potential using complimentary free energy is defined as,

$$\Psi(\Sigma_{ij}, T, f) = -\Delta G_{\text{chem}} - W_{\text{mech}} - W_{\text{inter}} + \Sigma_{ij} E_{ij}. \tag{1}$$

The total energy in Eq. (1) is the sum of the chemical free energy ΔG_{chem} , the interfacial free energy W_{inter}, and the mechanical energy W_{mech}. Interfacial free energy is considered negligible relative to the mechanical energy so it is ignored in the following. The term $\Sigma_{ij} E_{ij}$ represents the energy contribution from the macroscopic external stresses.

It is assumed that the chemical free energy is a linear function of the difference between the current temperature and the equilibrium transformation temperature, T_0, and is proportional to the martensite volume fraction, f. The final form of the complimentary free energy is determined using Eshelby's approach. For this approach, the local stress and strain fields respectively are the superposition of the average external stress field and the disturbance stress in the martensite variant and the superposition of the average elastic strain field and the transformation strain in the martensite variant. With these definitions, the mechanical energy is partitioned into two components:

$$\begin{aligned} W_{\text{mech}} &= \frac{1}{2V} \int_V \sigma_{ij} \varepsilon_{\text{ij}}^{\text{e}} \, \mathrm{d}V \\ &= \frac{1}{2} \Sigma_{ij} E_{ij}^{\text{e}} - \frac{1}{2V} \int_V \sigma_{ij}^{\text{dist}} \varepsilon_{\text{ij}}^{\text{tr}} \, \mathrm{d}V. \end{aligned} \tag{2}$$

The first term on the right hand side is the stored elastic energy, and the last term is an interaction energy term where V represents the martensite volume. Contributions to the mechanical energy due to interactions between martensite variants are reflected in the last term, expressed via an interaction energy. Patoor et al. [14]

used an interaction energy matrix, H^{mn} , to represent the interaction energy between two variants m and n, which can either be compatible or incompatible. The interaction energy is defined as.

$$H^{mn} = (\varepsilon_{ij}^{m} - \varepsilon_{ij}^{n})C_{ijkl}(I_{klrs} - S_{klrs}^{mn})(\varepsilon_{rs}^{m} - \varepsilon_{rs}^{n}). \tag{3}$$

For two compatible variants, the value of H^{mn} is low thus promoting the transformation. Conversely, the value of H^{mn} is high for incompatible variants thus hindering the transformation. Therefore, the complimentary free energy equation for a multi-variant martensitic transformation is given by

$$\Psi(\Sigma_{ij}T, f^{n}) = B(T_0 - T)\sum_{n} f^{n} + \frac{1}{2}\Sigma_{ij}E_{ij}^{\mathrm{e}} + \Sigma_{ij}\sum_{n}\varepsilon_{ij}^{n}f^{n} - \sum_{m,n}H^{mn}f^{n}f^{m}. \tag{4}$$

To arrive at the equation for the complimentary free energy, the total transformation strain is the sum of the average elastic and average transformation strains such that $E_{ij} = E_{ij}^{\mathrm{e}} + E_{ij}^{\mathrm{tr}}$. Also, the average transformation strain in a single crystal of parent phase is given by $E_{ij}^{\mathrm{tr}} = \sum_n \varepsilon_{ij}^{n} f^{n}$. The thermodynamic driving force acting on a martensite variant is obtained from partial differentiation of the complimentary energy equation with respect to f^{n} yielding

$$F^{n} = \frac{\partial\Psi(\Sigma_{ij}, T, f^{n})}{\partial f^{n}} = B(T_0 - T) + \Sigma_{ij}\varepsilon_{ij}^{n} - \sum_{m} H^{nm}f^{n}. \tag{5}$$

Dissipative aspects due to interfacial friction and defect generation are accounted for in a phenomenological way using a dissipative potential. From the second law of thermodynamics, the critical thermodynamic driving force required for the martensitic transformation is determined such that the transformation criteria becomes $F^{n} \geqslant \pm F_{\mathrm{c}}$. The positive or negative F_{c} is the driving force for the forward or reverse transformation respectively. When either transformation criterion is satisfied, the consistency condition is used to determine the volume fraction evolution rate of the transforming martensite variant. The macroscopic transformation strain is then calculated.

Previous formulations treat the martensite–austenite interfaces as coherent, thus relaxation of stored elastic strain energy is not accounted for. Our work advocates that plastic relaxation decreases the coherent interface strains leading to stored elastic strain energy dissipation. Dislocations generated as a result of plastic relaxation reduce the transformation strain according to $\varepsilon_1^{n} = \varepsilon^{n} - NAb/6V$ [22]. The variables in the equation are defined as follows: N is the number of dislocation loops; A is a geometric factor; b is the Burger's vector; and V is the volume of the single crystal martensite variant or CVP. The interaction energy is decreased for the reverse transformation; therefore, the reverse transformation requires an increased chemical contribution (e.g. increased temperature) to initiate the reverse transformation and bring it to completion. In this way, the model simulates how the driving force for the reverse transformation is reduced due to dissipation of stored elastic strain energy during the forward transformation. The modified transformation strain, ε_1^{n} , is approximated by $\varepsilon_1^{n} = \alpha\varepsilon^{n}$. Interaction energy is thus approximated using $H_1^{mn} = \alpha^2 H^{mn}$. Now the thermodynamic driving $\check{S}$ = force for the reverse transformation can be expressed as

$$F^{n} = B(T_0 - T) + \Sigma_{ij}\alpha\varepsilon_{ij}^{n} - \sum_{m}\alpha^2 H^{nm}F^{n}. \tag{6}$$

From the preceding analysis, an equation that characterizes the hysteresis exclusively attributed to stored elastic strain energy dissipation may be derived as follows. If the temperature at half the forward transformation strain is designated as T_{f}, then from Eq. (5)

$$T_{\mathrm{f}} = \frac{\Sigma_{ij}\varepsilon_{ij}^{n} - \sum_m H^{mn}F^{m} - F_c}{B} + T_0. \tag{7}$$

Similarly, if the temperature at half the reverse transformation strain is designated T_{r}, then from Eq. (6)

$$T_{\mathrm{r}} = \frac{\Sigma_{ij}\alpha\varepsilon_{ij}^{n} - \sum_m \alpha^2 H^{mn}F^{m} + F_{\mathrm{c}}}{B} + T_0. \tag{8}$$

Excluding the effects of frictional dissipation by ignoring F_{c}, the hysteresis exclusively attributed to stored elastic strain energy dissipation is characterized by

$$H_m = T_{\mathrm{r}} - T_{\mathrm{f}} = \frac{1}{B}\left[\sum_m H^{mn}F^{m}(1-\alpha^2) - \Sigma_{ij}\varepsilon_{ij}^{mn}(1-\alpha)\right]. \tag{9}$$

When α is equal to 1, no hysteresis exists ignoring frictional resistance to interfacial motion. By decreasing α with the level of external stress, there is a need for more overheating at higher external loads thus the hysteresis expands. The α term incorporates the influence of stored elastic strain energy dissipation resulting from plastic relaxation of coherent strains at austenite–martensite interfaces into the model. For simplification, each variant is assumed to undergo the same degree of relaxation. The predictions with the proposed model (to be presented later) correctly show the trend of increasing hysteresis with increasing external constant load.

4. Experimental results

4.1. Differential scanning calorimetry (thermal hysteresis without external stress)

The temperature hysteresis (marked as H_M in Fig. 3 for the aged cases) is defined as the temperature

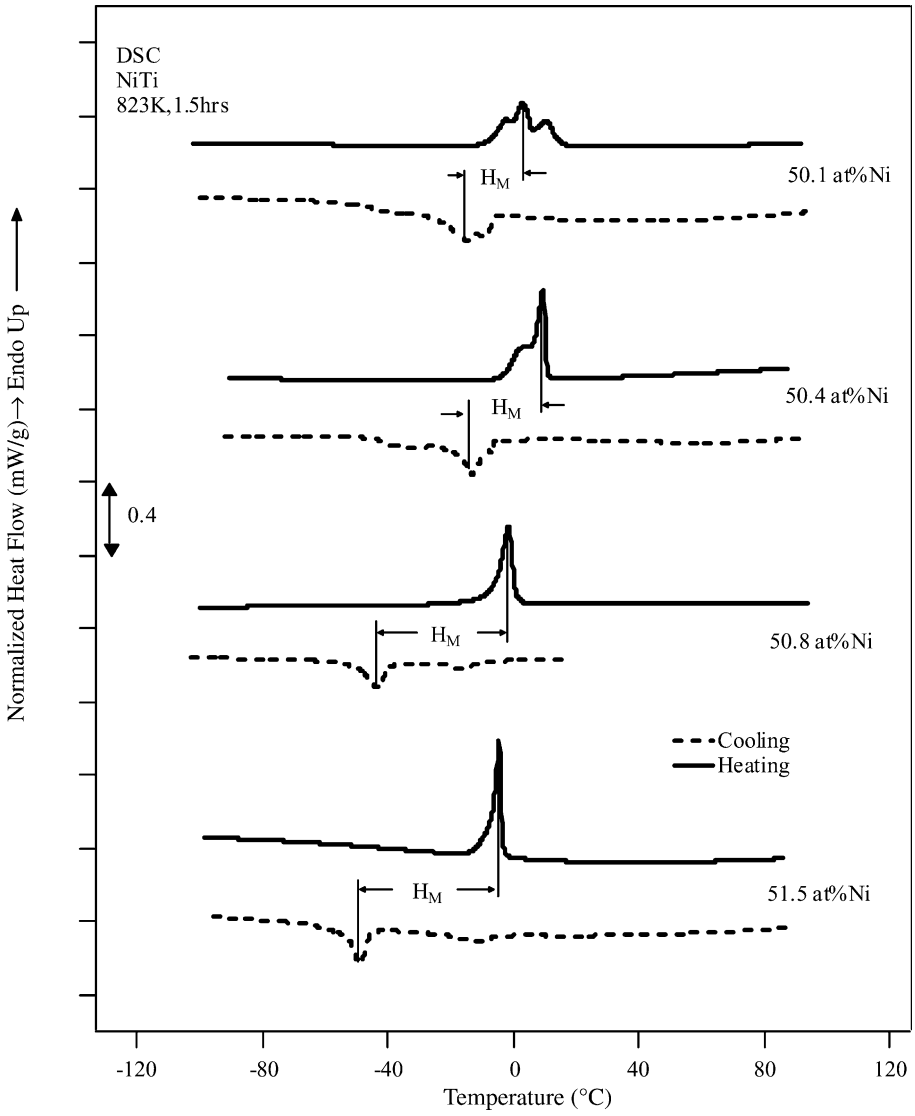

Fig. 3. DSC curves for aged NiTi alloys showing the temperature hysteresis (H_M) resulting from stress-free thermal cycling.

difference between the highest cooling (forward transformation) peak and the highest heating (reverse transformation) peak obtained from DSC (Fig. 3). Defining the hysteresis in a ' highest peak to peak' fashion provides an unambiguous method for comparison and avoids interpretation of multiple peaks observed which is beyond the scope of the current work. The temperature hysteresis shows an increase from 20 to 60 °C with increasing Ni content. The temperature hysteresis for solutionized Ti–50.8 and 51.5at.%Ni alloys could not be measured because the martensite start temperatures are below −200 °C. The temperature hysteresis width for the solutionized Ti–50.1 and 50.4at.%Ni alloys in the [1 2 3] orientation are slightly larger than that for the alloys in the aged condition (to be presented later). We also note the overall shift in transformation temperatures with changing Ni content. This shift is due to the additional internal stress fields associated with precipitates and changing matrix Ni concentration produced by precipitation.

4.2. Transmission electron microscopy

To characterize the volume fraction, size, and interparticle spacing of precipitates, TEM was utilized for both virgin and tested samples. In Fig. 4 the aged Ti–50.1at.%Ni and Ti–50.4at.%Ni alloys display a heterogeneous precipitate microstructure, but aged Ti–50.8at.%Ni Ti–51.5at.%Ni alloys have a homogeneous precipitate microstructure. From extensive TEM observations on aged Ti–50.1at.%Ni and Ti–50.4at.%Ni alloys, we observe that localized clusters of precipitates exist in some areas while no precipitates appeared in other areas, thus the precipitate microstructure is called heterogeneous. Conversely, the precipitates in the microstructures of the aged Ti–50.8 and 51.5at.%Ni alloys

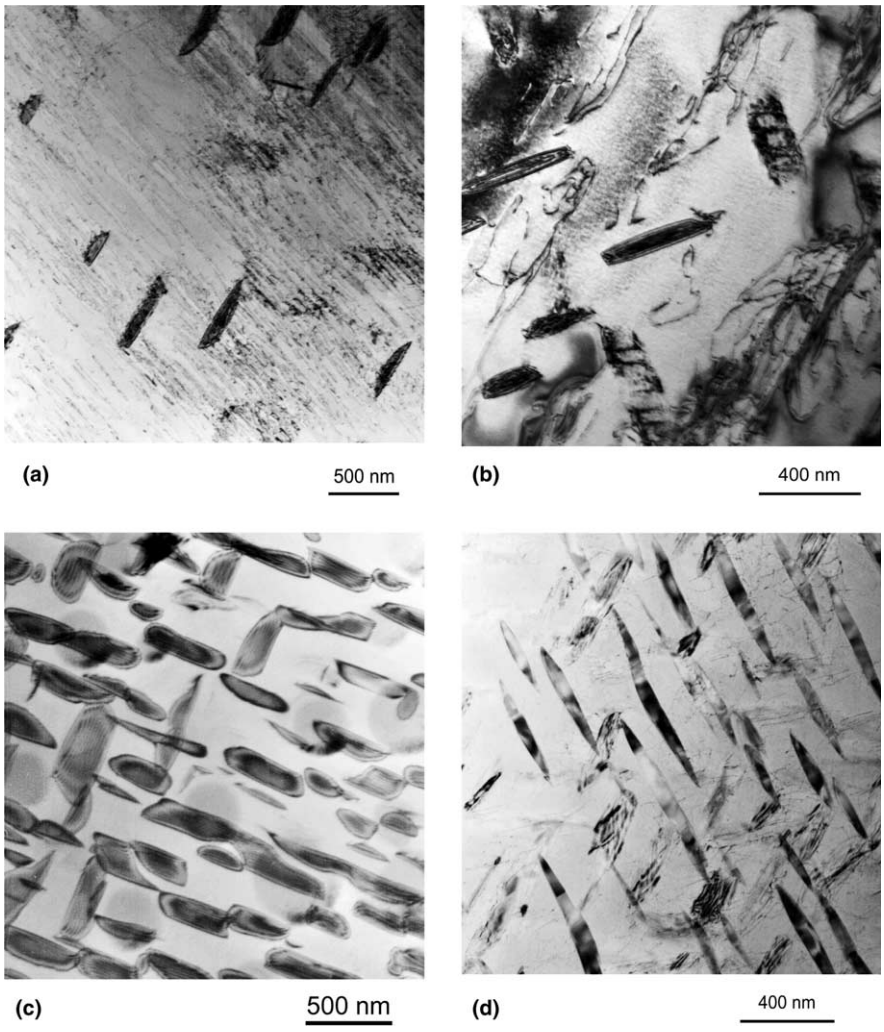

Fig. 4. TEM images of the aged (823 K, 1.5 h) precipitate microstructure in TiNi alloys. (a) 50.1at.%Ni, (b) 50.4at.%Ni, (c) 50.8at.%Ni, and (d) 51.5at.%Ni.

are uniformly spaced, thus we refer to this as a homogeneous precipitate microstructure.

4.3. Strain-temperature/pseudoelasticity (thermal/stress hysteresis under external stress)

An extensive series of experimental strain–temperature hysteresis curves are presented in Figs. 5–11 for different compositions and different single crystal orientations. We report on both solutionized and aged conditions for different levels of external stress. We illustrate the thermal hysteresis with the horizontal arrows (shown for 120 and 160 MPa) in Fig. 5. The thermal hysteresis is defined as the width of the strain-temperature loops measured at half the forward transformation strain. In Fig. 5 the theoretical strain for CVP formation and CVP+ detwinning strain are also included as dashed and solid lines respectively [12]. Figs. 5–7 correspond to strain–temperature curves for solutionized conditions while Figs. 8–11 provide results for aged cases. The maximum transformation strains for the Ti–50.1 and 50.4at.%Ni alloys are significantly higher than those for the Ti–50.8 and 51.5at.%Ni alloys. The low Ni alloys reach strain levels midway between the theoretical CVP strains and theoretical CVP plus detwinning strain. However, the transformation strains for the Ti–50.8 and 51.5at.%Ni alloys fall well short of the theoretical CVP strain.

We observe recognizable differences between the slopes of high Ni alloy (Figs. 10 and 11) and low Ni alloy (Figs. 5–9) strain–temperature curves. For the Ti–51.5at.%Ni alloy in Fig. 11, we distinguish a discontinuous slope for the forward transformation curve, whereas the reverse transformation slope of the low Ni alloys is continuous. The high level of external stress (225 MPa) for the initial thermal cycle does not expose the R-phase effect for the Ti–50.8at.%Ni alloy in Fig. 10. The reverse transformation curves exhibit a continuous

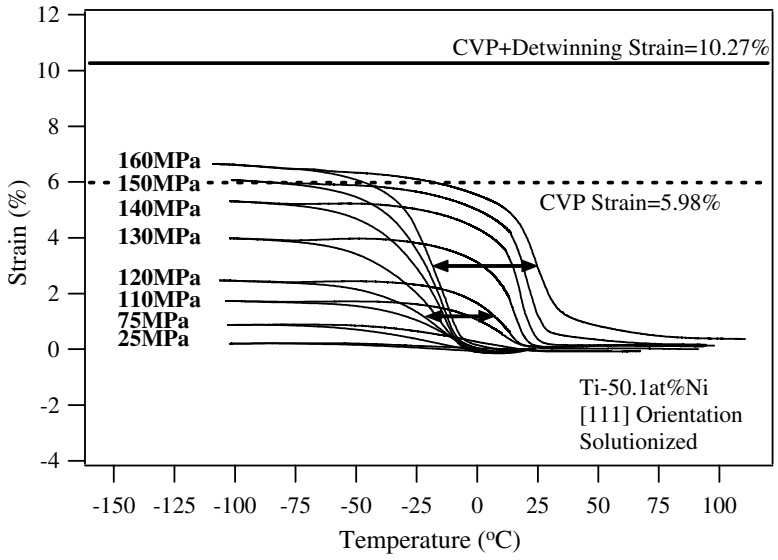

Fig. 5. Strain–temperature curves resulting from thermal cycling under constant tensile load with an increasing applied load in successive thermal cycles for a solutionized Ti–50.1at.%Ni single crystal in the [1 1 1] orientation.

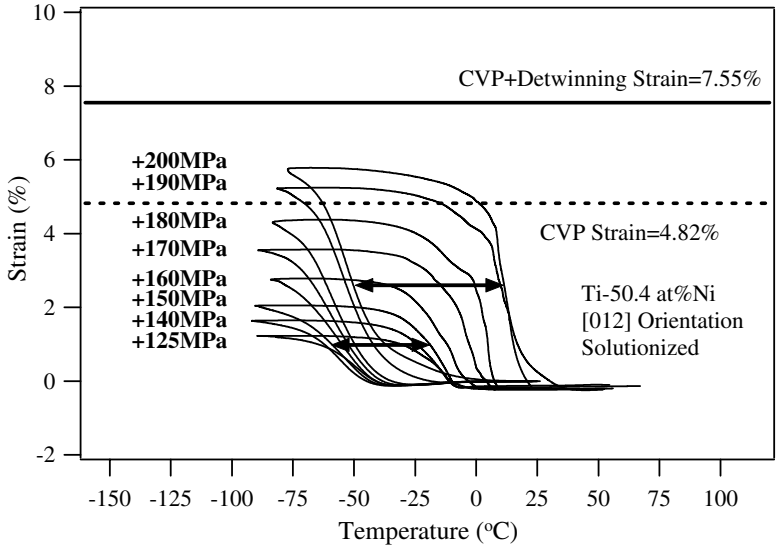

Fig. 6. Strain–temperature curves resulting from thermal cycling under constant tensile load with an increasing applied load in successive thermal cycles for a solutionized Ti–50.4at.%Ni single crystal in the [0 1 2] orientation.

slope regardless of Ni content. Though the forward and reverse curves are parallel for the low Ni alloys (Figs. 5–9), the curves are not parallel for the high Ni alloys (Figs. 10 and 11). Finally, we observe that the slopes of the forward transformation curves for the aged low Ni alloys are steeper than those of the high Ni alloys. This is clearly obvious comparing the curves for thermal cycles at 50 MPa, which are sharp for the Ti–50.1 and 50.4at.%Ni alloys (Figs. 8 and 9) and shallow for the Ti–51.5at.%Ni alloy (Fig. 11).

Based on the strain–temperature curves, we summarize in Fig. 12(a) how the hysteresis grows with increasing external stress for aged and solutionized low Ni compositions. The hysteresis levels of near 20 °C corresponding to small external stress levels (less than 25 MPa) are in agreement with the DSC results. However, as the external tensile stress is increased to near 200 MPa the hysteresis levels increase to as high as 80 °C. The trends from 50.1at.%Ni and 50.4at.%Ni are similar so all the results are superimposed in Fig. 12(a). We also note that a similar variation in hysteresis was observed in the presence of single ([1 2 3]) vs. multiple martensite variants ([1 1 1] and [0 1 1] cases). There have not been many systematic investigations of thermal hysteresis for low Ni NiTi alloys and such growth in the hysteresis has not been elucidated in early work. Although their

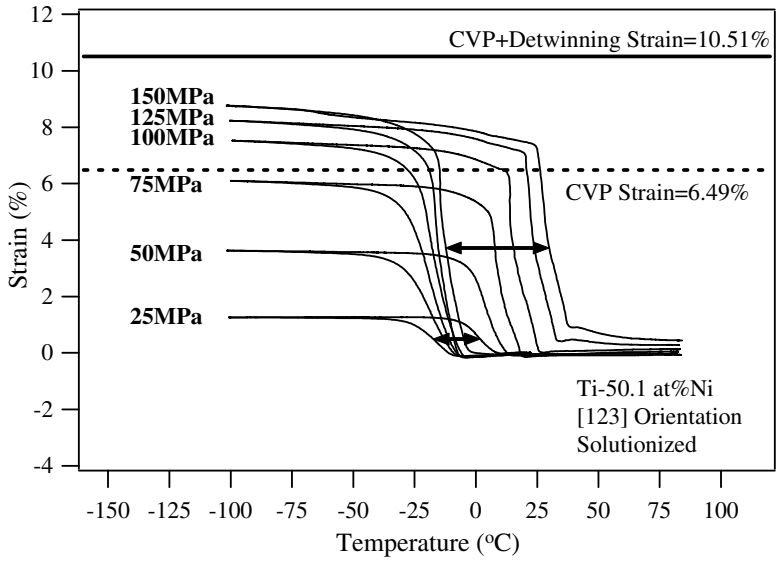

Fig. 7. Strain–temperature curves resulting from thermal cycling under constant tensile load with an increasing applied load in successive thermal cycles for a solutionized Ti–50.1at.%Ni single crystal in the [1 2 3] orientation.

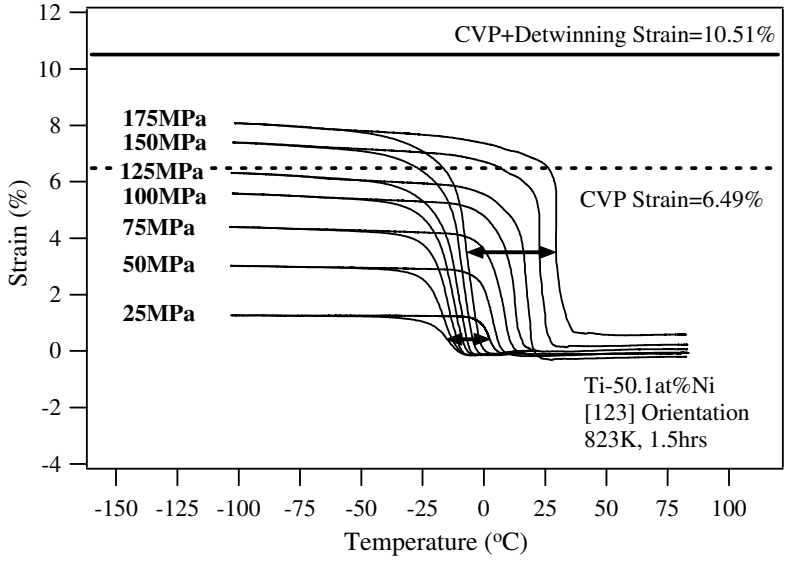

Fig. 8. Strain–temperature curves resulting from thermal cycling under constant tensile load with an increasing applied load in successive thermal cycles for an aged Ti–50.1at.%Ni single crystal in the [1 2 3] orientation.

studies were not focused on the hysteresis, the experiments of Gabry et al. [17] exhibit a growing hysteresis accompanying an increasing external stress for a polycrystalline Ti–48.7at.%Ni alloy.

The thermal hysteresis results are summarized for the higher Ni NiTi alloys in Fig. 12(b). Unlike the trend in low Ni case, the temperature hysteresis decreases with increasing external stress for high Ni cases. In addition to the 50.8at.%Ni and 51.5at.%Ni results, experimental results from three other studies are superimposed in Fig. 12(b). Although they did not investigate the nature of the hysteresis, the works of Gabry et al. [17], Nomura et al. [24], and Miyazaki et al. [25], also show a shrinking hysteresis. In their experiments, the materials were polycrystalline Ti–50.5at.%Ni, Ti–51.2at.%Ni and Ti–51.5at.%Ni alloys respectively. Finally, it is observed upon comparing Fig. 12(a)–(b) that the hysteresis for high Ni alloys is larger than that for low Ni alloys at stresses less than or equal to 75 MPa.

To gain further insight into the hysteresis behavior, pseudoelastic stress–strain response was studied for the two extreme cases, 50.1at.%Ni and 51.5at.%Ni. Analogous to the thermal hysteresis, the stress hysteresis is defined at the middle of the loading stress plateau of the

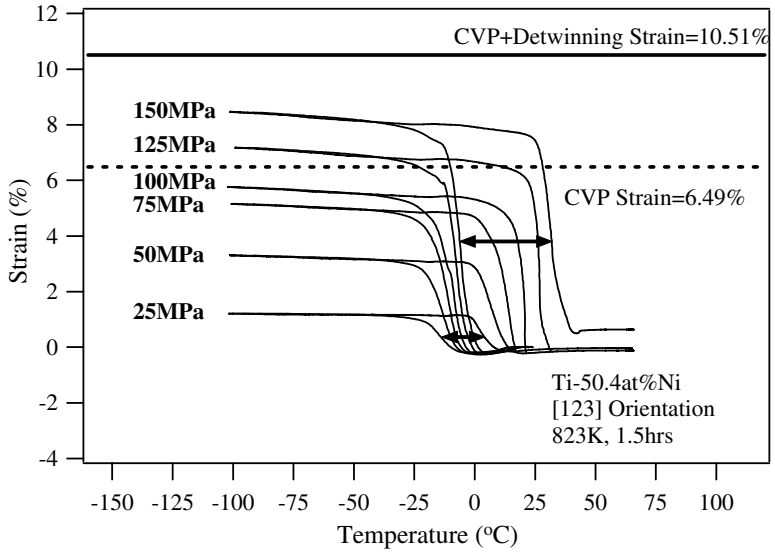

Fig. 9. Strain–temperature curves resulting from thermal cycling under constant tensile load with an increasing applied load in successive thermal cycles for an aged Ti–50.4at.%Ni single crystal in the [1 2 3] orientation.

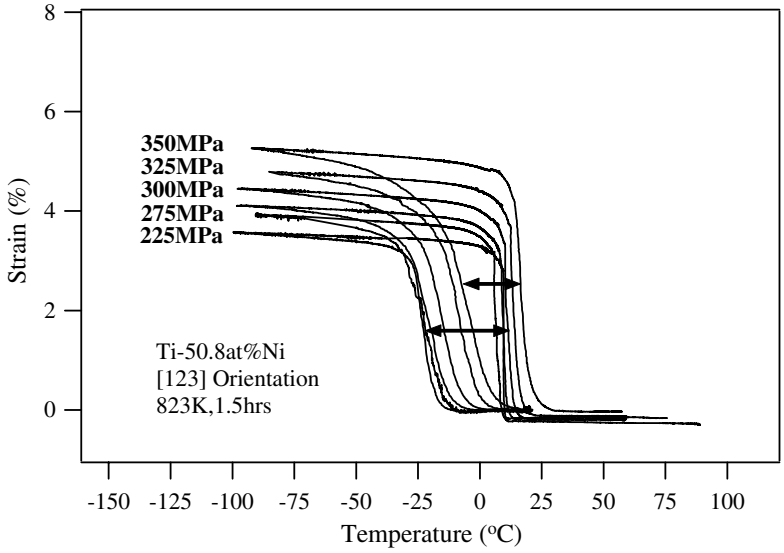

Fig. 10. Strain–temperature curves resulting from thermal cycling under constant tensile load with an increasing applied load in successive thermal cycles for an aged Ti–50.8at.%Ni single crystal in the [1 2 3] orientation.

hysteresis loops (see arrows in Fig. 13). In Fig. 13(a) the stress hysteresis increased with increasing isothermal test temperatures for low Ni alloys and decreased for high Ni alloys. We note that the deformation temperatures are slightly different for the two cases while the absolute values of transformation stresses are much higher for the 51.5at.%Ni case. The pseudoelastic stress hysteresis in the works of Chumlyakov et al. [26] and Liu and Galvin [27] exhibit stress dependencies that follow the trends observed in the current work. Liu and Galvin's results for polycrystals show that the stress hysteresis increases with increasing test temperature for a Ti–50.2at.%Ni alloy. On the other hand, the results of Chumlyakov et al. for single crystals show that the stress hysteresis decreases for a Ti–51at.%Ni alloy with increasing temperature.

5. Discussion of results

5.1. Martensite morphology – homogeneous vs. heterogeneous precipitate microstructure

We anticipate that the martensite in solutionized microstructures thermally cycled with no external loading will mainly consist of SAGs of martensite CVPs. When

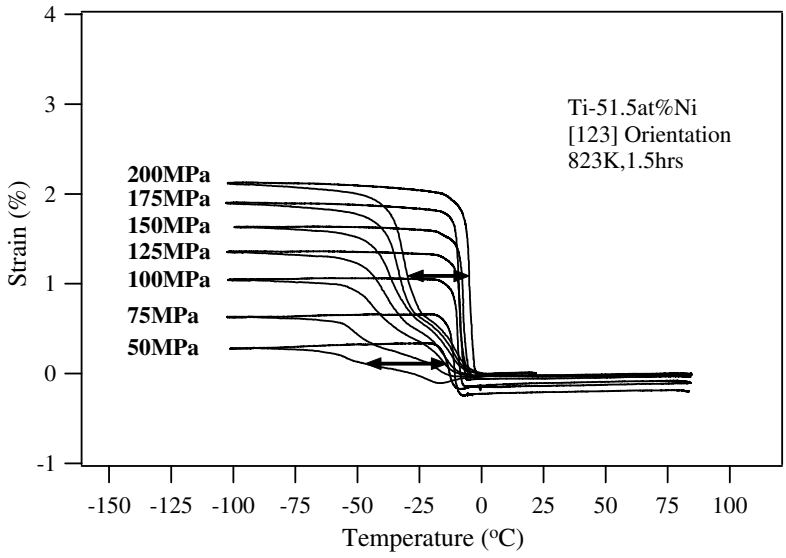

Fig. 11. Strain–temperature curves resulting from thermal cycling under constant tensile load with an increasing applied load in successive thermal cycles for an aged Ti–51.5at.%Ni single crystal in the [1 2 3] orientation.

external stress is applied, favorably oriented martensite CVPs within SAGs grow. The volume fraction of external stress-induced martensite grows when the external stress is amplified. In aged materials, contrasts in the martensite morphology depend on the precipitate microstructure. The precipitate stress fields are highly localized in the heterogeneous precipitate microstructures of the aged Ti–50.1at.%Ni and Ti–50.4at.%Ni alloys. Therefore, the martensite phase should consist of a high volume fraction of self-accommodating groups away from precipitate stress fields and a small volume fraction of precipitate stress-induced martensite. On the contrary, the homogenous precipitate microstructure of the aged Ti–50.8at.%Ni Ti–51.5at.%Ni alloys yields a highly uniform internal stress field. Consequently, the volume fraction of martensite will consist mainly of variants favorably oriented to the internal stress.

We envisage evolution of three groups of martensites during thermal cycling of aged materials under constant stress: (1) SAGs, (2) external stress-induced martensite, and (3) precipitate stress-induced martensite. With increasing external stress, martensite CVPs within SAGs that are favorable to both the precipitate and external stress grow at the expense of others. Further increases in external stress, enlarge the volume fraction of external stress-induced martensite, causing the relative amount of precipitate stress-induced martensite to decrease accordingly.

5.2. Thermal hysteresis without external stress

Hysteresis expansion with higher Ni content in Fig. 3 is explained considering differences in precipitate volume fractions and the ensuing martensite microstructures. For high Ni alloys, the volume fraction of martensite should aptly consist of a significant amount of precipitate stress-induced martensite. Influential relaxation of elastic strain energy could result due to the interaction of different precipitate stress-induced martensite variants promoting hysteresis expansion. Conversely, the martensite phase in low Ni alloys likely contains a considerable amount of SAGs plus highly localized precipitate-induced martensite. Since SAGs minimize stored elastic strain energy and interactions between these SAGs and oriented martensite are limited, the degree of energy dissipation is potentially considerably less than that of high Ni alloys. Frictional work dissipated due to resistance to interfacial motion is expectedly lower in low Ni alloys because of the sparser precipitate stress fields and low matrix strength associated with lower Ni contents. However, significant frictional resistance could exist in high Ni alloys because of their increased matrix strength and homogeneous precipitate microstructure. The aforementioned differences in frictional resistance also promote a wider hysteresis for aged high Ni alloys compared to aged low Ni alloys.

The wider hysteresis for solutionized low Ni alloys compared to the alloys in the aged condition (Fig. 12(a)) is attributed to stored elastic strain energy and friction dissipation. For aged alloys, the contribution of stored elastic strain energy to the reverse transformation would increase due to sheared precipitate stress fields, which decreases the necessary overheating and thus the hysteresis. The Ni content of the aged austenite matrix is lower than that of the solutionized state due to precipitation. An accompanying weaker frictional resistance supports the smaller hysteresis for aged low Ni alloys.

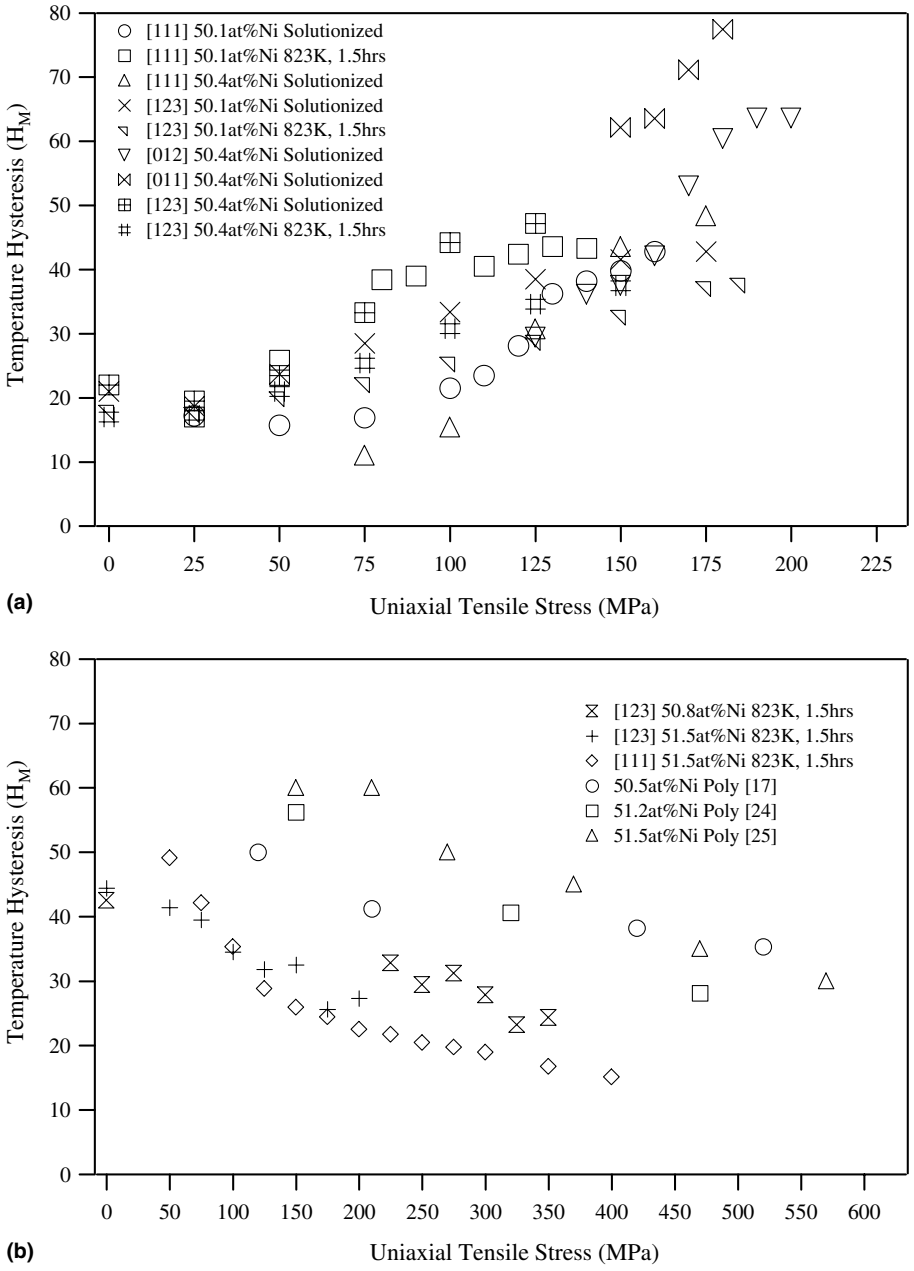

Fig. 12. Comparison of hysteresis evolution with increasing applied stress: (a) low and (b) high Ni concentration NiTi alloys.

We note that the multiple peaks in 50.1at.%Ni are attributed to an inhomogeneous precipitate microstructure. For low Ni single-crystals, our scanning electron microscopy studies (not reported here) exposed the existence of dendrites and low angle tilt boundaries. Therefore, compositional variations develop in low Ni alloys, where precipitate volume fraction has spatial variation. In that case, the phase transformation proceeds through multiple steps. Arguments based on microstructural heterogeneity in aged polycrystals have been made by Khalil-Allafi et al. [28] also displaying a multistep transformation. In their case, precipitates nucleated near grain boundaries while grain interiors exhibited precipitate-free zones. The nominal composition of high Ni alloys in our study produces a high volume fraction of homogenously distributed precipitates thus negating the effects of compositional variations. Therefore, the peaks for higher Ni alloys are widely separated with no apparent overlaps.

5.3. Thermal/stress hysteresis under external stress

Contrasts in the continuity of forward transformation slopes for low (Figs. 8 and 9) and high Ni (Fig. 11)

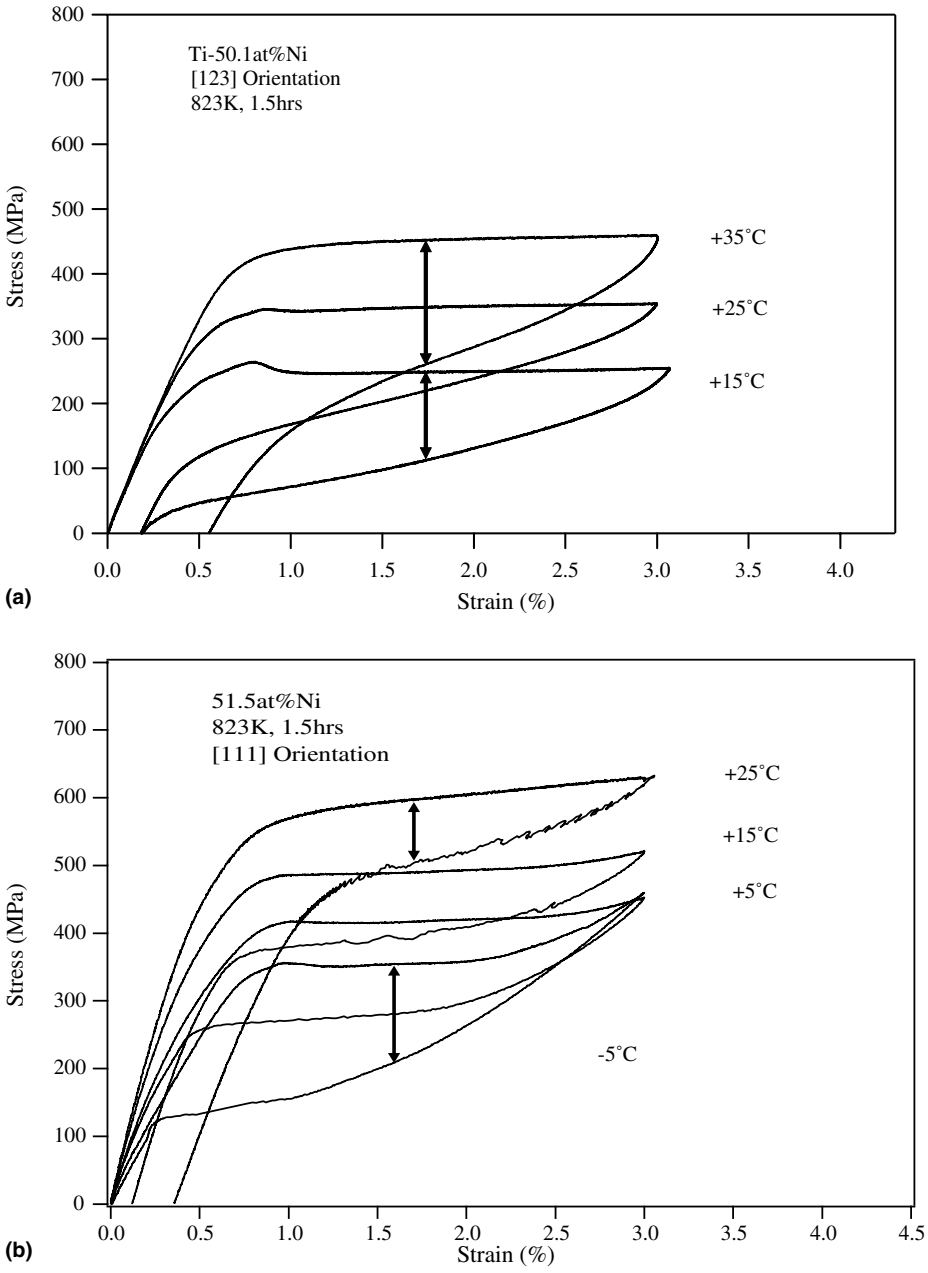

Fig. 13. Comparison of stress hysteresis evolution with increasing temperature for (a) low and (b) high Ni concentration NiTi alloys.

alloys correlate well with the DSC peaks shown in Fig. 3. Two distinct thermal events give rise to the first and second DSC cooling peaks for high Ni alloys and the peaks are widely separated. We associate the first cooling peak with the R-phase transformation, thus the first slope in Fig. 11 is attributed to the R-phase transformation. The second slope and DSC cooling peak arise from the subsequent R-phase to B19′ martensite transformation. On the contrary, the forward and reverse transformation for low Ni alloys yield an amalgamation of peaks that appear to occur during broad thermal events. Accordingly, the strain–temperature curves in Figs. 8 and 9 exhibit a continuous slope on cooling and heating. Therefore, for the case of transformation under load, the intermediate transformation steps are most likely bypassed for the 50.1 and 50.4at.%Ni alloys. Likewise, the reverse transformation for the Ti–51.5at.%Ni alloy gives rise to one DSC peak and a continuous strain–temperature slope. The parallelism of strain–temperature curves may correspond with the separation of DSC peaks; in low Ni alloys, the curves are parallel while the curves are non-parallel in the high Ni cases.

The differentiation between steep and shallow inclinations of the strain–temperature curves for low and high Ni alloys (Figs. 8–11) illustrates the different levels

of elastic strain energy associated with the forward transformation. Stored elastic strain energy contributions must increase significantly for high Ni alloys compared to low Ni alloys. We anticipate that this is the case for the homogeneous precipitate microstructure because of internal strain fields in the martensite. A higher volume fraction of precipitate stress-induced martensite is anticipated in high Ni alloys. Elastic strains associated with this oriented martensite elicit more elastic strain energy as well.

We now discuss the difference between the stress dependence of the hysteresis in low Ni alloys compared to high Ni alloys. This difference can be argued considering relaxation of coherency stresses at inter-phase boundaries and reduction of stored elastic strain energy. Roitburd and Kurdjumov [2] argue that plastic deformation is the main cause of irreversible effects and that contributions from other dissipative mechanisms are small compared to plastic accommodation. Kokorin et al. [9] conclude that the size of the hysteresis is controlled by the degree of relaxation of coherent stresses at the inter-phase boundaries. The matrix is softer in low Ni alloys than in high Ni alloys thus plastic accommodation of the transformation strains is expected to occur more readily in low Ni alloys. As shown in Figs. 5–9, low Ni alloys reach transformation strain levels midway between the theoretical CVP strains and theoretical CVP plus detwinning strain. Twin boundaries become more mobile and detwinning occurs more readily in low Ni alloys as the external stress increases. An increase in external stress produces more severe plastic relaxation of coherent stresses at martensite–austenite interfaces. As a result, the level of stored elastic strain is lowered hence its contribution to the reverse transformation decreases causing the hysteresis to increase.

Dislocations emitting from martensite–austenite interfaces are shown in Fig. 14. We also note that the dislocations bow out such that the spacing of the loops is of the order of twin thickness within the martensite. The role of large number of dislocation loops is to reduce the internal stress in the martensite domains. It follows that there will be less elastic strain energy available to aid the reverse transformation, which evokes hysteresis growth. In addition to the dislocation generation at the austenite–martensite phase boundary, planar dislocations and tangled dislocations are observed in the austenite domains. The dislocation density in austenite is far greater in the Ti–50.1at.%Ni alloy compared to that of the Ti–51.5at.%Ni (compare Fig. 15(a) vs. (d)). Since the dislocation density is expected to increase as the external stress increases, the frictional resistance to phase boundary motion will also increase due to a hardening effect. The increased frictional resistance will amplify hysteresis expansion.

We note that for the $\langle 0\,1\,0\rangle\{1\,1\,0\}$ and $\langle 0\,1\,0\rangle\{1\,0\,0\}$ slip systems in the B2 phase the RSSF for [0 0 1] orientation should be zero [12]. Therefore, plastic deformation should be severely curtailed in the [0 0 1] case. The experiments on the [0 0 1] crystal orientation can be utilized to check the basis of our hypothesis of hysteresis growth due to plastic flow. Indeed, as shown in Fig. 16(a) and (b), the hysteresis did not vary with external stress for both aged and solutionized Ti–50.4at.%Ni alloys of [0 0 1] orientation. This behavior

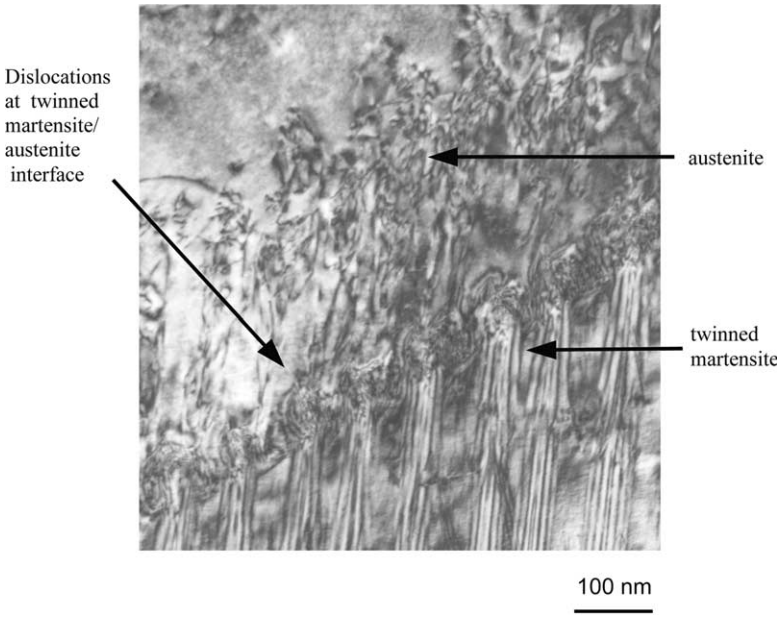

Fig. 14. Solutionized Ti–50.1at.%Ni single crystal of [1 1 1] orientation thermally cycled under constant load with load increased for successive thermal cycles showing dislocations being emitted from martensite-interface at internal twin boundaries.

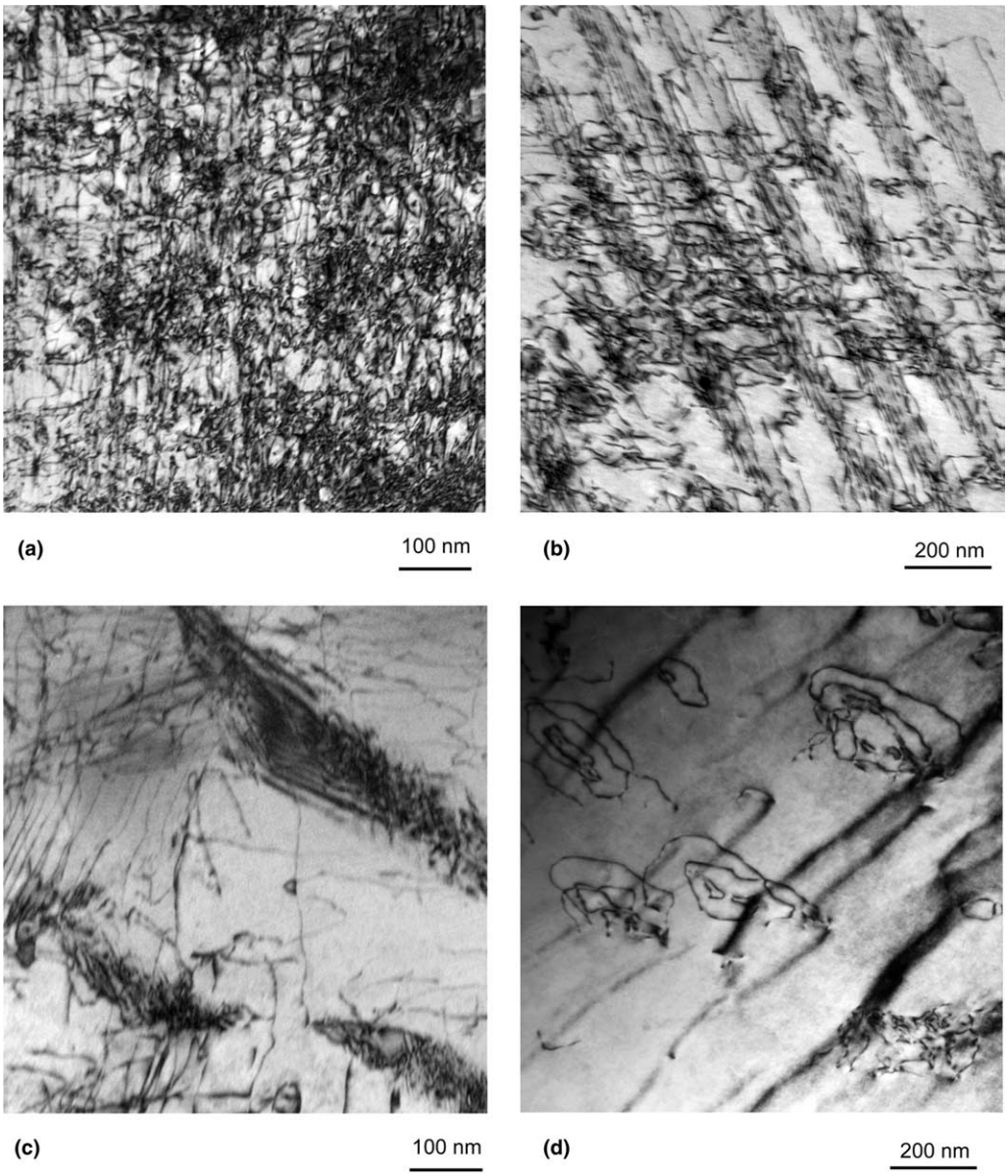

Fig. 15. (a) Solutionized Ti–50.1at.%Ni single crystal of [1 1 1] orientation showing high dislocation density with tangles and some planar alignment. (b) Solutionized Ti–50.4at.%Ni single crystal of [1 2 3] orientation showing preferentially aligned planar dislocations. (c) Aged (823 K, 1.5 h) Ti–50.8at.%Ni single crystal of [1 2 3] orientation showing precipitates and some dislocations. (d) Aged (823 K, 1.5 h) Ti–51.5at.%Ni single crystal of [1 2 3] orientation showing precipitates and a few dislocations.

occurred despite the wide range of stresses examined (from 125 to 230 MPa). The TEM images in Fig. 17 confirm that minimal dislocation activity was detected in solutionized and aged Ti–50.4at.%Ni alloys in the [0 0 1] orientation. In summary, the Ti–50.4at.%Ni [0 0 1] orientation results support the assertion that plastic relaxation is the dominant dissipative mechanism in low Ni alloys. It should be noted that there is a small hysteresis increase in the solutionized case, whereas, the hysteresis remains exactly constant for the aged case. Fig. 17(b) shows some increased dislocation activity compared to Fig. 17(a), which can be attributed to age hardening (e.g. precipitates block dislocation motion as observed in Fig. 17(a)). This may be the reason for the slight hysteresis increase with external stress for the solutionized alloy.

For high Ni alloys, the hysteresis shrinks because dissipation remains constant with increasing external stress due to matrix strength, whilst more elastic strain energy storage accompanies elevated transformation strain. The external stress does not induce considerable changes in dislocation evolution because the strain hardening associated with slight increases in dislocation density is rather small. It follows that frictional

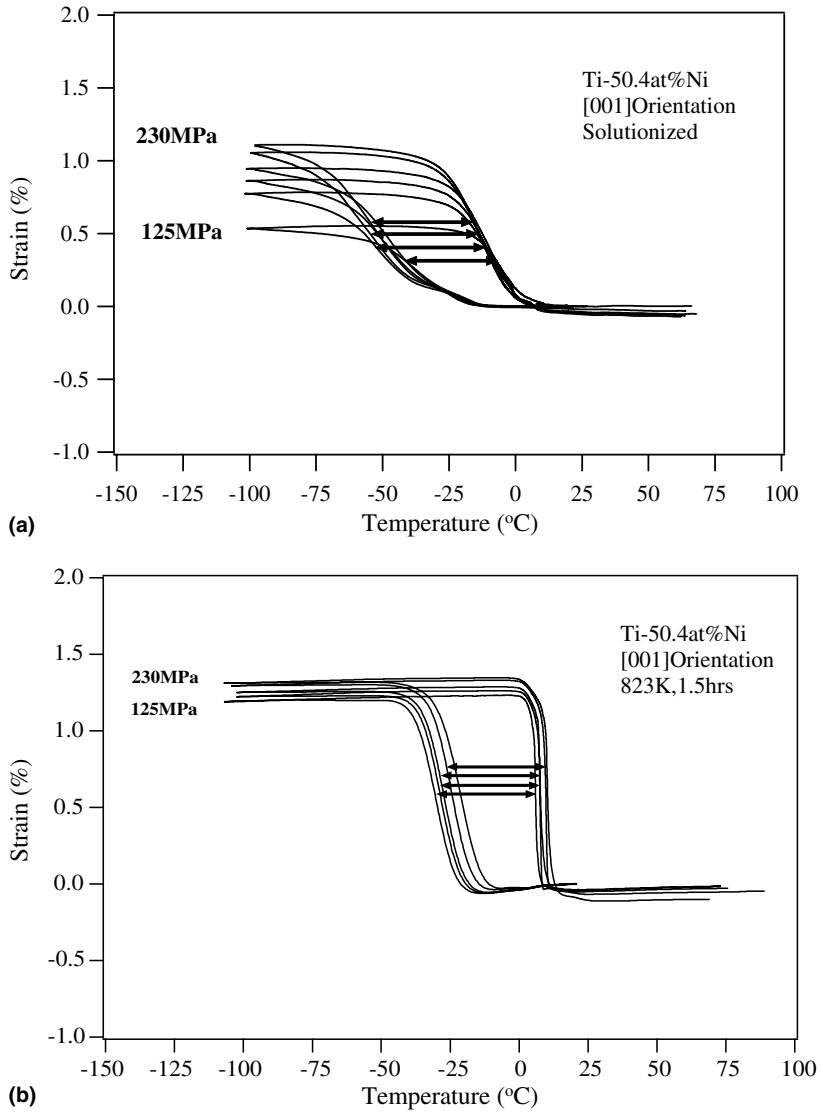

Fig. 16. Experiments demonstrating constant strain–temperature hysteresis with increasing stress (stress was increased in +15 MPa increments within stresses on the plots) for (a) solutionized and (b) aged Ti–50.4at.%Ni [0 0 1] single crystals. Several curves omitted for clarity.

resistance to interfacial motion will not change significantly as the external stress increases. Recently it has been proposed that compound twinning occurs in aged high Ni content alloys which leads to lower transformation strains compared to the predominant Type II twinning for aged low Ni content alloys [29,30]. Consequently, the transformation strains for the Ti–51.5at.%Ni and 50.8at.%Ni alloys fall well short of the theoretical CVP strain. Since the matrix exhibits higher slip resistance for high Ni alloys and twin boundary motion and detwinning are suppressed, plastic accommodation does not accompany transformation strain. Indeed, Fig. 15(c) and (d) reveal considerably less dislocation activity in the Ti–50.8at.%Ni and Ti–51.5at.%Ni alloys. When external stress is present, the volume fraction of external stress-induced martensite (oriented martensite due to external stress) grows. This is accompanied by large increases in stored elastic strain energy. This alone may cause the hysteresis to decrease with increasing external stress since plastic relaxation is insignificant and the elastic strain energy contribution that assists the reverse transformation increases as the external stress increases.

Similar to the hysteresis increase with higher Ni content observed in DSC results, the hysteresis measurements in high Ni alloys is larger than that of low Ni alloys at stresses less than or equal to 75 MPa (Fig. 12). Likewise, the martensite morphologies are expected to be similar owing to the low external stress. Therefore, the hysteresis contrasts are attributed to the rationale given earlier for the increase in the DSC hysteresis with increasing Ni content.

Strain–temperature curves calculated using the current model are presented in Fig. 18. The model, presented earlier in the paper, accounts for plastic

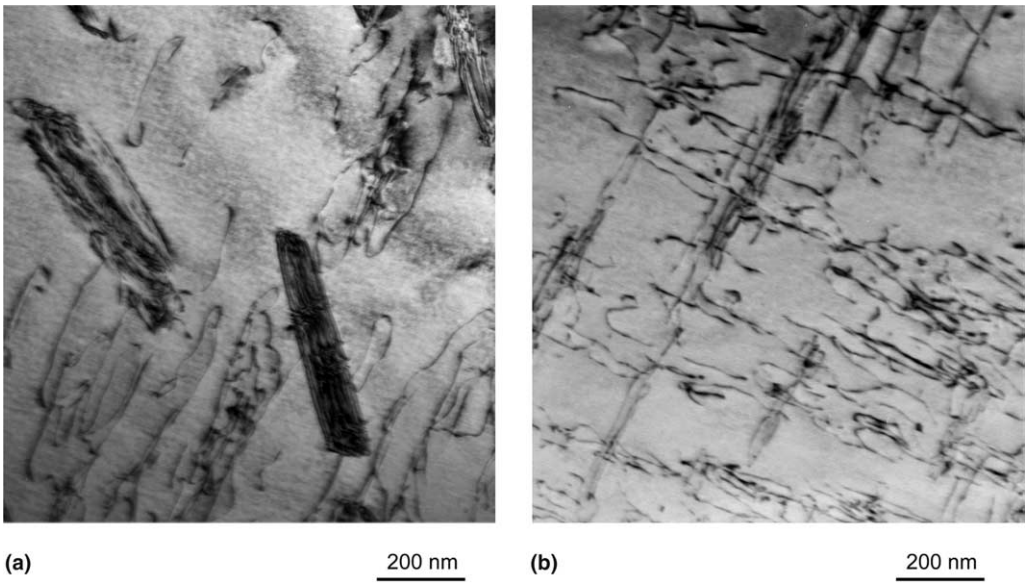

Fig. 17. TEM of the Ti–50.4at.%Ni single crystal alloys of [0 0 1] orientation in Fig. 16: (a) the aged condition showing planar dislocation arrays along with precipitates that may inhibit dislocation motion and (b) the solutionized condition showing two orientations of planar dislocation arrays.

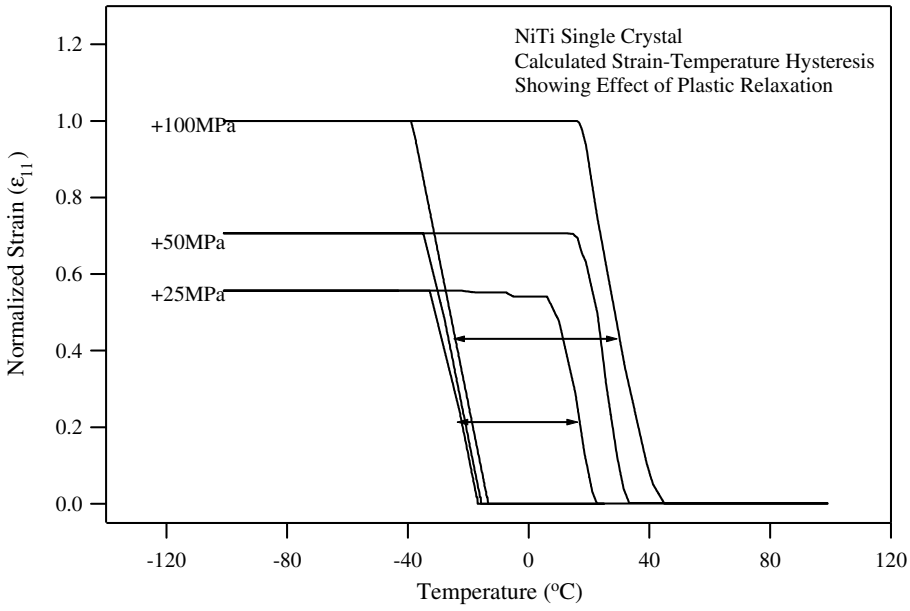

Fig. 18. Calculated strain–temperature curves that consider plastic relaxation of coherent stresses at austenite/martensite interfaces.

relaxation. In the modeling, plastic relaxation effects are amplified as the external stress is increased for successive thermal cycles. Therefore, the results exhibit an expanding temperature hysteresis with increasing external stress consistent with the low Ni alloy results. The model simulates other features of the experimental strain temperature curves as well. One example is that transformation temperatures shift to higher values as the external stress is raised. Another example is that higher transformation strains are achieved in conjunction with an incremental increase in external stress. This is a consequence of increased volume fraction of favorably oriented variants with increasing external stress.

6. Conclusions

Several conclusions are drawn from this study.

1. The temperature hysteresis increases with increasing external stress for aged (823 K, 1.5 h) and solution-

ized Ti–50.1at.%Ni and Ti–50.4at.%Ni (low Ni) alloys, but it decreases with increasing stress for the aged Ti–50.8at.%Ni and Ti–51.5at.%Ni (high Ni) alloys. The changes in hysteresis were substantial, from 20 °C to as high as 80 °C for the low Ni case, and from 60 to 15 °C for the high Ni case.

2. Under external stress, the plastic relaxation of coherency strains, shown via bowed dislocation segments over the entire austenite–martensite interfaces, was the most potent energy dissipative mechanism. The plastic relaxation at the austenite–martensite interfaces produces a reduction of elastic strain energy. The increased dissipation produces substantial hysteresis growth with increasing external stress in low Ni alloys. The only exceptions are the experiments in [0 0 1] orientation, which do not display the hysteresis growth due to the lack of slip systems.
3. Hysteresis shrinkage with increased external stress in the high Ni alloys is attributed to negligible dissipation due to a homogenous precipitate microstructure and a harder matrix. In this case, the elastic strain energy stored during the forward transformation increases with increasing external stress. Since dissipation is negligible and the stored elastic strain energy assists the reverse transformation, less chemical energy (i.e. less heating) will be required to initiate and complete the reverse transformation.
4. A thermo-micromechanical formulation that considers plastic relaxation of mechanical elastic energy captures the hysteresis growth with increasing external stress. The model provides explicit expressions for the forward and reverse transformation temperatures incorporating the role of external stress, transformation strain, and the variant–variant interaction terms.

Acknowledgements

This work was partially supported by the Air Force Office of Scientific Research, Grant No. F49620-01-1-0136 and the National Science Foundation Grant, CMS-0332824. The assistance of Prof. H. S. Woo with DSC experiments is gratefully acknowledged.

References

[1] Ortin J, Planes A. Thermodynamic analysis of thermal measurements in thermoelastic martensitic transformations. Acta Metall Mater 1998;36(8):1873–89.
[2] Roitburd AL, Kurdjumov GV. The nature of martensitic transformation. Mater Sci Eng 1979;39:141–67.
[3] Salzbrenner RJ, Cohen M. On the thermodynamics of thermoelastic martensitic transformations. Acta Metall 1979;27:739–47.
[4] Delaey L, Ortin J, Van Humbeeck J. Hysteresis effects in martensitic non-ferrous alloys. In: Proceedings of the Phase Transf 87. The Institute of Metals, 1988. p. 60–6.
[5] Olson GB, Cohen M. Thermoelastic behavior in martensitic transformations. Scripta Metall 1975;9:1247–54.
[6] Hornbogen E. The effect of variables on martensitic transformation temperatures. Acta Metall 1985;33:595–601.
[7] Van Humbeeck J, Aeronoudt E, Delaey L, Li Lu, Verguts H, Ortin J. Hysteretic transformation behaviour of shape memory alloys. Revue Phys Appl 1988;23:557–64.
[8] Ortin J, Planes A. Thermodynamics and hysteresis behaviour of thermoelastic martensitic transformations. J de Phys IV 1991;1(C4):13–23.
[9] Kokorin VV, Gun'ko LP, Shevchenko OM. Degree of tetragonality of the crystal lattice of martensite and a hysteresis of the transformation in Fe–Ni–Co–Ti alloys. Phys Met Metall 1992;74(5):502–5.
[10] Kokorin VV, Kozlova LE, Titenko AN. Temperature hysteresis of martensite transformation in aging Cu–Mn–Al alloy. Scripta Mater 2002;47:499–502.
[11] Kozlova LE, Kokorin VV, Titenko AN. The effect of aging on the temperature hysteresis of martensitic transformation in the Cu–Mn–Al alloy. Phys Met Metall 2002;94:295–7.
[12] Sehitoglu H, Hamilton R, Canadinc D, Zhang XY, Gall K, Karaman I. Detwinning in NiTi Alloys. Metall Mater Trans A 2002;33:5–13.
[13] Sehitoglu H, Karaman I, Anderson R, Zhang X, Gall K, Maier HJ. Compressive response of NiTi single crystals. Acta Mater 2000;48:3311–26.
[14] Patoor E, Eberhardt A, Berveiller M. Micromechanical modelling of superelasticity in shape memory alloys. In: Pitman Research Notes in Mathematics Series, 1993;296:38–54.
[15] Niclaeys C, Ben Zineb T, Arbab-Chirani S, Patoor E. Determination of the interaction energy in the martensitic state. International Journal of Plasticity 2002;18:1619–47.
[16] Gall K, Sehitoglu H. The role of texture in tension/compression asymmetry in polycrystalline NiTi. International Journal of Plasticity 1999;15:69–92.
[17] Gabry B, Lexcellent C, No VH, Miyazaki S. Thermodynamic modeling of the recovery strains of sputter-deposited shape memory alloys Ti–Ni and Ti–Ni–Cu films. Thin Solid Films 2000;372:118–33.
[18] Sun QP, Hwang KC. Micromechanics modelling for the constitutive behavior of polycrystalline shape memory alloys. – I. Derivation of general relations. J Mech Phys Solids 1993;41(1):1–17.
[19] Huang M, Brinson LC. A multivariant model for single crystal shape memory alloy behavior. J Mech Phys Solids 1998;46(8):1379–409.
[20] Zhang S, McCormick PG. Thermodynamic analysis of shape memory phenomena – II. Modelling. Acta Mater 2000;48:3091–101.
[21] Bo Z, Lagoudas DC. Thermomechanical modeling of polycrystalline SMAs under cyclic loading. Part I: Theoretical derivations. Int J Eng Sci 1999;37:1089–140.
[22] Johnson WC, Lee JK. A dislocation model for the plastic relaxation of the transformation strain energy of a misfitting spherical particle. Acta Metall Mater 1983;31(7):1033–45.
[23] Ashby MF, Johnson L. On the generation of dislocations at misfitting particles in a ductile matrix. Philos Mag 1969;20:1009–22.
[24] Nomura K, Miyazaki S, Ishida A. Effect of plastic strain on shape memory characteristics in sputter-deposited Ti–Ni thin films. J de Phys IV 1995;5(C8):695–700.
[25] Miyazaki S, Normura K, Zhirong H. Shape memory effect and superelasticity developed in sputter-deposited Ni–Ti thin films. In: Pelton AR, Hodgson D, Duerig T, editors. Proceedings of the First International Conference on Shape Memory and Superelastic Technologies, California, 1994. p. 19–29.

[26] Chumlyakov YI, Efimenko SP, Kireeva IV, Panchenko EY, Sehitoglu H, Gall K. Effects of shape memory and superelasticity in aged TiNi single crystals. Tech Phys 2001;381(5):610–3.
[27] Liu Y, Galvin SP. Criteria for pseudoelasticity in near-equiatomic NiTi shape memory alloys. Acta Mater 1997;45:4431–9.
[28] Khalil-Alafi J, Dlouhy A, Eggeler G. Ni4Ti3-precipitation during aging of NiTi shape memory alloys and its influence on martensitic phase transformations. Acta Mater 2002;50: 4255–74.
[29] Sehitoglu H, Karaman I, Zhang X, Viswanath A, Chumlyakov Y, Maier HJ. Shape memory and pseudoelastic behavior of 51.5at.%Ni–Ti single crystals in solutionized and overaged state. Acta Mater 2001;49:3609–20.
[30] Liu Y, McCormick PG. Thermodynamic analysis of the martensitic transformation in NiTi – I. Effect of heat treatment on transformation behaviour. Acta Metall Mater 1994;42(7): 2401–6.